Influence of Discrete Defects on Observed Acoustic−Phonon Dynamics in Layered Materials Probed with Ultrafast Electron Microscopy

Published as part of The Journal of Physical Chemistry virtual special issue "Time-Resolved Microscopy".

Spencer A. Reisbick, Yichao Zhang, and David J. Flannigan*

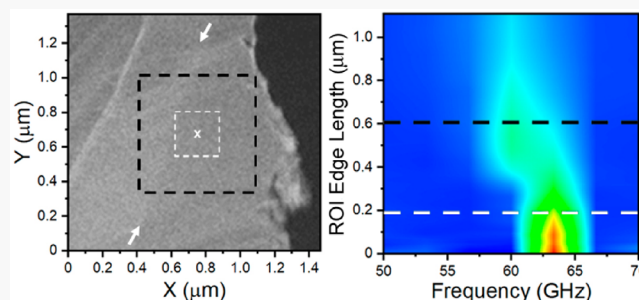Cite This: *J. Phys. Chem. A* 2020, 124, 1877−1884

Read Online

ACCESS | Metrics & More | Article Recommendations | SI Supporting Information

ABSTRACT: The structural anisotropy of layered materials leads to disparate lattice responses along different crystallographic directions following femtosecond photoexcitation. Ultrafast scattering methods are well-suited to resolving such responses, though probe size and specimen structure and morphology must be considered when interpreting results. Here we use ultrafast electron microscopy (UEM) imaging and diffraction to study the influence of individual multilayer terraces and few-layer step-edges on acoustic-phonon dynamics in $1T\text{-}TaS_2$ and $2H\text{-}MoS_2$. In TaS_2, we find that a multilayer terrace produces distinct, localized responses arising from thickness-dependent c-axis phonon dynamics. Convolution of the responses is demonstrated with ultrafast selected-area diffraction by limiting the probe size and training it on the region of interest. This results in a reciprocal-space frequency response that is a convolution of the spatially separated behaviors. Sensitivity of phonon dynamics to few-layer step-edges in MoS_2 and the capability of UEM imaging to resolve the influence of such defects are also demonstrated. Spatial frequency maps from the UEM image series reveal regions separated by a four-layer step-edge having 60.0 GHz and 63.3 GHz oscillation frequencies, again linked to c-axis phonon propagation. As with ultrafast diffraction, signal convolution is demonstrated by continuous increase of the size of the selected region of interest used in the analysis.

INTRODUCTION

Femtosecond (fs) photoexcitation of transition metal dichalcogenides (TMDs) produces a nonequilibrium condition characterized by lattice and structural responses influenced by electronic structure, crystal structure, and discrete nanoscale morphology.[1−13] Strong absorption of visible and near-infrared photons initially leads to rapid structural changes both within and between the basal planes of few- and multilayer specimens within the first few picoseconds (ps) due to carrier−carrier and carrier-atom scattering.[4,7,10−12] The resulting transient thermo-elastic response produces a time-dependent modulation of local strain at discrete lattice discontinuities (*e.g.*, vacancies, impurities, interfaces, and step-edges). Relaxation is achieved through launch of low-frequency (tens of GHz) acoustic phonons, which in the case of *ab*-plane modes initially propagate away from discrete discontinuities over tens to hundreds of ps.[2,3,5,11] The anisotropic bonding leads to distinctly different phonon behaviors characterized by discrete vibrational frequencies that are linked to the intrinsic sound velocities.[3,8,11] Indeed, charge-ordering, as in TMDs support-ing charge density waves, may lead to anomalous bonding interactions along specific crystallographic directions that then

modulate phonon velocities and transient responses for certain phases. Melting and reformation of these phases, especially in the presence of order-directing structures and morphologies, may then manifest in the low-frequency responses. Ultimately, system relaxation continues over time via excitation of whole-flake mechanical eigenmodes which oscillate over time scales ranging from tens of nanoseconds to microseconds or more, depending upon the precise nature of the dissipative channels and boundary conditions of the specimen geometry.[5]

The low-frequency, speed-of-sound behaviors of photo-excited propagating acoustic phonons in TMDs, combined with the sensitivity of the detailed responses to discrete structure and morphology, renders such phenomena especially amenable to study with femtosecond electron imaging and diffraction.[2,6,8,9,14−19] These two experimental methodologies are generally differentiated by the manner in which electrons
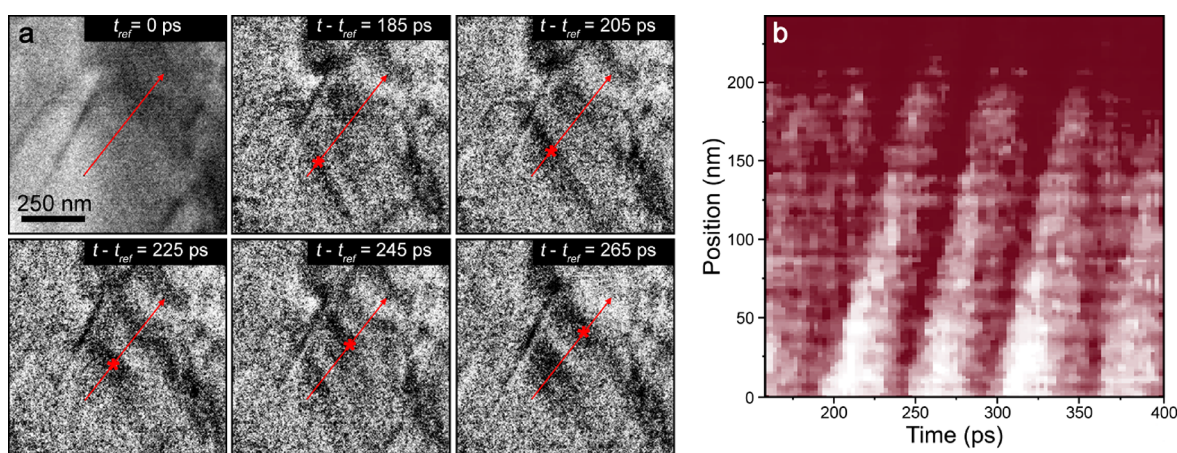
Figure 1. UEM imaging of fs photoexcited acoustic−phonon propagation in multilayer TaS$_2$. (a) UEM bright-field reference image at experimental time zero (t_{ref} = 0 ps) and subsequent difference images ($t − t_{ref}$) acquired at select times following the onset of observable dynamics. The precise time following onset of dynamics at which each frame was acquired is shown in the upper-right corner of each difference image. For reference, dark regions in the difference images arise from a transient increase in Bragg scattering due to a propagating lattice disturbance. The red star in the difference images tracks the approximate position of an individual phonon wavefront moving in the direction indicated by the red arrow. See Video S1 for observed acoustic-phonon dynamics in this particular TaS$_2$ specimen region, as obtained with UEM. (b) Space-time contour plot generated from a region of interest (ROI) oriented parallel to the red arrow shown in the individual panels in part a. Each dark, tilted band represents an individual phonon wavefront, the velocity of which is denoted by the slope (direction and speed). Here, the average speed was observed to be 4.2 ± 0.2 nm/ps, where the error is one standard error of the fit to the bands (see the Supporting Information and Figure S1). For reference, the 0 nm position corresponds to the tail of the red arrow in part a.

scattered by the specimen are collected, precisely as is the case for conventional transmission electron microscopy (TEM). Simply, the type of information obtained depends upon if either the image or the diffraction plane of the object (specimen) is projected onto the detector. These are complementary methods, providing both unit-cell-level, spatially averaged lattice information and nanoscale to microscale, spatially resolved morphological information. Accordingly, ultrafast electron microscopes (UEMs) based on conventional TEM technology are well-suited for the study of TMD phonon and strain-wave dynamics owing to the spatiotemporal scales on which these behaviors occur.[6,20−23] In essence, UEM extends conventional TEM imaging, diffraction, and spectroscopic capabilities to the femtosecond time scale.[22,24−27] Thus, one can (for example) probe TMD unit-cell and structural/morphological dynamics from femtoseconds to milliseconds and angstroms to micrometers by simply switching between lens-excitation conditions to change the information selected to be the object of the projection system.

Owing to the discrete nature and localized influence of lattice and structural imperfections on phonon dynamics in TMDs, combined use of UEM imaging and diffraction is desirable for developing a comprehensive understanding of such phenomena. Here we demonstrate this by identifying and directly imaging distinct acoustic-phonon dynamics in 1T-TaS$_2$ and 2H-MoS$_2$ (TaS$_2$ and MoS$_2$ from here forward) with fs electron imaging in UEM. We show that distinct interlayer phonon frequencies arise in specific specimen regions separated by crystal step-edges with heights as small as one unit cell. Further, we illustrate how distinct vibrational frequencies across the step-edges are convoluted in ultrafast selected-area electron diffraction measurements and how spatiotemporal differentiation of those same modes can be performed with UEM imaging. This latter study serves as an explicit illustration of how probe size and sampled specimen area dictate the overall observed response.

■ MATERIALS AND METHODS

Thicknesses of the TaS$_2$ and MoS$_2$ flakes were determined with electron energy-loss spectroscopy (EELS), and the presence and locations of multilayer terraces and few-layer step-edges were determined with high-angle annular dark-field scanning TEM (HAADF-STEM). All EELS data and HAADF-STEM images were acquired with an FEI G2 TITAN aberration-corrected TEM (Thermo Fisher Scientific). Spectra were acquired pixel-by-pixel over the region of interest (ROI), and the flake thickness within a particular ROI was determined by finding the ratio of the counts within the zero-loss peak to the counts within the bulk plasmon peak (see the Supporting Information for details).[28−30]

All UEM experiments were conducted using an FEI Tecnai Femto UEM (Thermo Fisher Scientific) operated at 200 kV. In situ specimen photoexcitation and generation of probe photoelectron packets were performed with a 6 W, diode-pumped, solid-state Yb:KGW (1.03 μm) fs pulsed laser (PHAROS, Light Conversion). Pulse durations measured with a scanning autocorrelator (GECO, Light Conversion) were 300 fs full-width at half-maximum (fwhm) exiting the laser. Repetition rates were selected using a pulse picker and typically were in the range of tens of kHz. Second-harmonic generation (515 nm) was performed with a harmonics module (HIRO, Light Conversion) customized to have collinear emission. The fourth harmonic (258 nm) used for generating the probe photoelectron packets in the UEM gun region was performed separately. The photoelectron source was a 50 μm diameter, graphite-encircled LaB$_6$ cathode (Applied Physics Technologies), and a 1.5 mm diameter Wehnelt aperture and a 1.25 mm diameter condenser aperture were used to increase the overall beam current. A 1 m mechanical bearing linear delay stage (PRO165LM, Aerotech) was used to control the relative time of arrival of the photoelectron packets and the pump laser pulses at the specimen. Either 1.2 or 2.4 eV photons were used to pump the specimen, and an estimated
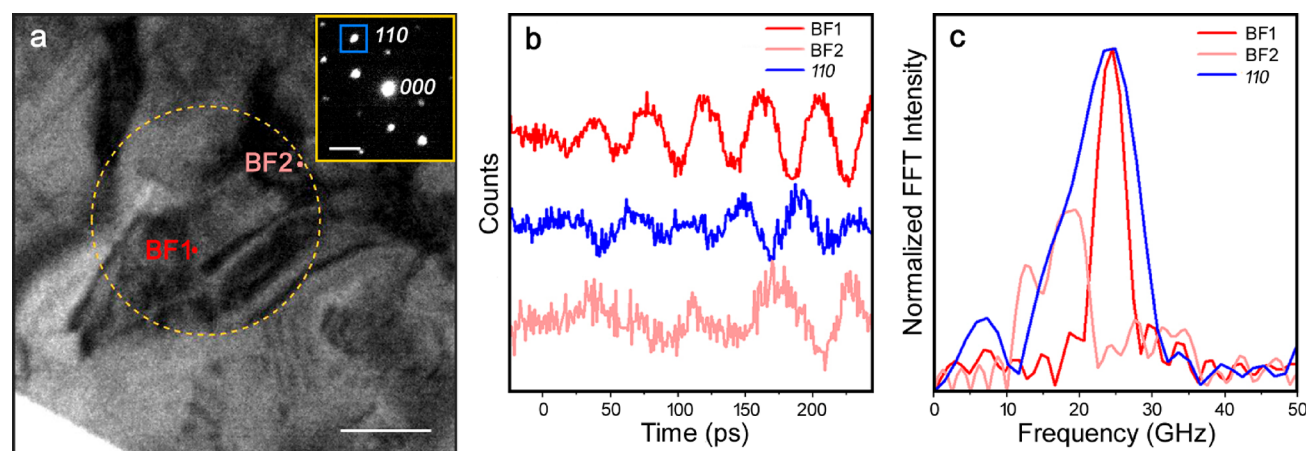
Figure 2. UEM imaging and selected-area diffraction (SAED) of a common ROI in TaS$_2$. (a) UEM image of a specimen ROI with corresponding SAED pattern (inset) generated from the area within the yellow dashed circle. The colored dots labeled BF1 and BF2 (BF = bright-field) mark positions at which imaging dynamics were quantified (see the Supporting Information and Figure S2). The counts behavior of the *110* Bragg spot (indexed and marked with a blue square in the inset) was also quantified and compared to the select-position imaging dynamics. Scale bars represent 500 nm and 3 nm^{-1}. See Video S2 for a UEM video of the imaging dynamics in this particular specimen region. (b) Transient counts behavior of the *110* Bragg spot from the selected specimen area compared to the imaging dynamics at BF1 and BF2. The plots are offset for clarity. Note that the time-varying background counts were subtracted from the time-varying counts of the *110* spot in order to better isolate the oscillatory behavior. (c) FFTs of the corresponding time-varying signals in part b normalized to the overall peak intensity. Fits to the peaks for BF1 and BF2 return frequencies of 24.9 GHz and 17.5 GHz, respectively, while the FFT of the response of the *110* Bragg peak is a convolution of the two, as evidenced by the shoulder to the lower-frequency side of the peak. The FFTs were calculated using a sampling window from −25 to +249 ps at 1 ps steps. The *x*-axis was generated by creating a vector from 1 to the length of the input data set divided by 2 and then multiplied by the sampling frequency and divided by the length. The calculations were done using the FFTW subroutine in MATLAB.[35]

spot size of 100 μm fwhm at the specimen ensured uniform spatial illumination over the few-micrometer ROIs studied here. Pump fluences of 2 and 4 mJ/cm^2 were used for the TaS$_2$ experiments, while 0.8 mJ/cm^2 was used for the MoS$_2$ experiments. For all experiments reported here, experimental time zero is defined as the moment at which dynamics were first observed in the UEM imaging or diffraction series. For all TaS$_2$ experiments, images and diffraction patterns were acquired with a Gatan Orius SC200B 4 megapixel fiber-coupled CCD camera, while a Gatan OneView 16 megapixel CMOS camera, modified to enable continuous signal acquisition, was used for all MoS$_2$ experiments. Where necessary, image alignment of the UEM image series was performed using the template-matching plugin in ImageJ.[31]

The TaS$_2$ and MoS$_2$ specimens were prepared via mechanical exfoliation from bulk crystals (HQ Graphene and 2D Semiconductors, respectively) using adhesive tape and following previously reported methods.[2,3,5] An optical microscope was used to inspect the exfoliated pieces prior to attaching the adhesive tape to an NaCl single crystal (Ted Pella). The crystal was then washed repeatedly with isopropyl alcohol and heated at 95 °C in order to dissolve the adhesive. A solution of 4 wt % PMMA in methoxybenzene was then applied dropwise to the surface of the NaCl crystal supporting the TMD flakes and annealed for 10 min. The PMMA/TMD film was then floated off of the NaCl crystal using deionized water and was captured with a copper TEM grid (Ted Pella; 1000 mesh for TaS$_2$ and 2000 mesh for MoS$_2$). The grid and film were rinsed repeatedly with acetone to remove the PMMA and then allowed to dry for several hours in air at room temperature.

■ RESULTS AND DISCUSSION

In situ photoexcitation of TMDs, archetypal semiconducting materials, and metal nanocrystals produces contrast waves in

UEM bright-field imaging arising from excitation of coherent acoustic phonons.[2,3,5,11,18] Shown in Figure 1a is an example of in-plane propagating acoustic phonons in TaS$_2$ (see Video S1). As previously observed in other materials systems, the phonon wavetrain emerges from an extended structural discontinuity (here, a vacuum-crystal interface). The wavetrain propagates perpendicular to, and away from, the defect at approximately the in-plane speed of sound. Velocity is determined via image analysis and the generation of space-time contour plots (Figure 1b and Figure S1). Details of these methods and descriptions of the physical processes at work have been previously reported (see also the Supporting Information).[11,18] Here, phonons comprising the wavetrain propagate with an in-plane speed of 4.2 ± 0.2 nm/ps, as determined from the space-time contour plot. While reasonable, this speed is higher than basal-plane velocities of 3 nm/ps measured using neutron scattering and ultrasonic pulses in relatively large TaS$_2$ crystals.[32,33] Though not the specific subject of this work, potential origins of this difference are mentioned below.

Owing to the anisotropic bonding in TMDs, phonon behaviors in the *ab* crystallographic plane are distinctly different from those along the *c*-axis layer-stacking direction, as imaged with UEM.[3,11] While the in-plane modes produce propagating contrast waves in the UEM image series, the *c*-axis modes cause an oscillatory but nonpropagating response. Though the images are a 2D projection, *c*-axis dynamics can be accessed by simply tilting the specimen such that the [001] crystallographic direction is not parallel to the incident electron wave vector.[2,3,9,11] Thus, phonon propagation along the *c*-axis produces a spatially stationary but oscillatory response, with the frequency of oscillation being indicative of the interlayer speed of sound (as dictated by the elastic tensor values) and the local specimen thickness. Indeed, frequency shifts (*i.e.*, differences in wavenumber) of bend−contour oscillations in nanoscale crystal regions of MoS$_2$ arising from
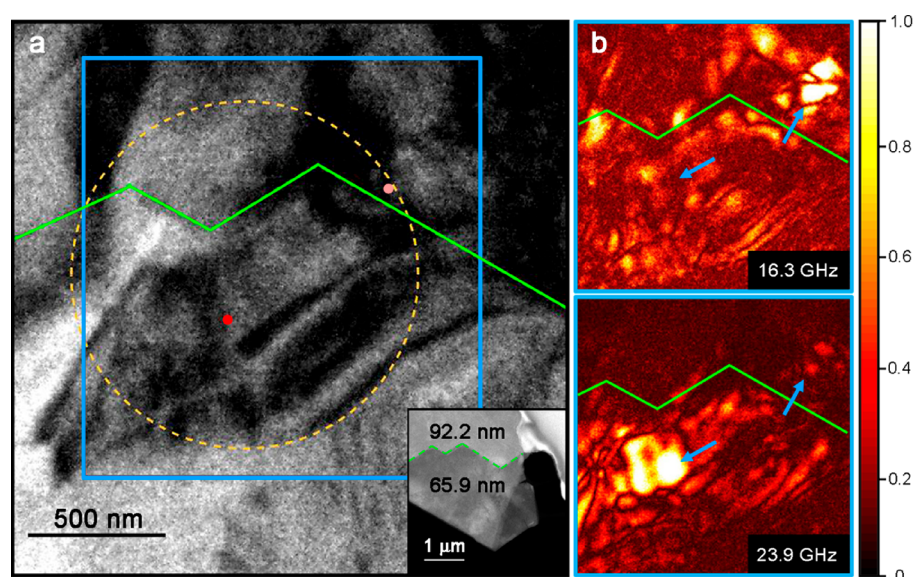
Figure 3. Origin of disparate phonon dynamics in a terraced TaS$_2$ specimen. (a) Select UEM bright-field image of the TaS$_2$ ROI analyzed in Figure 2. The specimen region isolated with the selected-area aperture (yellow dashed circle) and the BF1 and BF2 positions (red and pink dots, respectively) are shown for reference. The green line marks the approximate position of a multilayer crystal terrace, as determined with HAADF-STEM imaging (see the Supporting Information and Figures S3−S5). The blue box denotes the region analyzed in panel b. The inset shows a lower-magnification HAADF-STEM image of the ROI, wherein the terrace is apparent and marked with a green dashed line. The thickness of each region separated by the terrace is labeled (92.2 nm and 65.9 nm). (b) Spatial frequency maps at 16.3 GHz and 23.9 GHz (upper and lower panel, respectively). Units of the color map are counts normalized to the maximum overall image counts. The approximate position of the terrace is denoted in each panel with a green line. Blue arrows mark the approximate positions of the maximum intensities in each panel; the arrows are in the same position in each panel.

thickness variations of one unit cell have been spatiotemporally identified and resolved with UEM (more on this below).[11]

Sensitivity of observed phonon dynamics to a few molecular layers arising from discrete crystal step-edges suggests the nature of the overall measured signal critically depends upon the size of the probed specimen region. That is, the measured response will depend upon both the material crystal structure and the precise specimen morphology from which scattered electrons are collected. This is conceptually the same as translating the specimen in the *xy*-plane in a conventional TEM; differences in static structure and morphology produce changes in the observed scattering pattern as the specimen is translated within the beam.[34] With UEM, it is the photo-induced changes of an otherwise stationary specimen that produces the observed response. If additionally there are structural and morphological variations *within* the probed region that cause distinct dynamics, sampling from the entire region will produce a response that is a convolution of the disparate behaviors. Thus, spatially localized dynamics will not be resolved.

An explicit example of the discussion above is shown in Figure 2. Here, an ROI displaying distinct dynamics at localized spots in TaS$_2$ was probed with both UEM bright-field imaging and selected-area electron diffraction (SAED). With UEM imaging, two 16 pixel by 16 pixel spots separated by approximately one micrometer, but displaying distinctly different oscillatory dynamics, were identified (labeled BF1 and BF2 in Figure 2a). A fast Fourier transform (FFT) of the oscillatory, time-varying signals returned frequencies of 24.9 and 17.5 GHz for BF1 and BF2, respectively (Figure 2b,c), suggesting a difference in local thickness arising from a spatially abrupt change in layer number between the two spots (discussed below). Depending upon probe size and defect

density, the presence of both oscillatory behaviors should be detected in ultrafast SAED measurements of ROIs containing such structural features. This is indeed the case, as shown here. A UEM SAED scan of the ROI containing both BF1 and BF2 was conducted, and the time-varying counts and associated FFT of the *110* Bragg spot was found to be a convolution of the 24.9 GHz and 17.5 GHz oscillations (Figure 2b,c). Note that the time-varying response for the *110* spot is phase shifted in time by $\phi(t) = \pi$ relative to the imaging response owing to the inverse relationship between real and reciprocal space. It is also worth noting that for SAED, the postspecimen selected-area aperture effectively sets the probe size to the imaged aperture size for parallel-beam illumination (approximately 1.5 μm diameter in Figure 2).

In order to confirm that the origin of the spatial frequency difference highlighted in the UEM bright-field image series summarized in Figure 2 is due to a crystal terrace and thus a difference in thickness, a combination of HAADF-STEM imaging, EELS thickness mapping, and pixel-by-pixel spatial frequency mapping of the UEM bright-field image series was employed. The results of this multimodal study are summarized in Figure 3. The contrast in the HAADF-STEM image allowed for determination of the approximate position of the crystal terrace traversing the ROI in the TaS$_2$ specimen (denoted with green lines in the Figure 3 panels). By combining this with EELS thickness mapping, the height of the terrace was found to be 26 nm (see the Figure 3a inset). Further, a pixel-by-pixel spatial frequency map of a select region of the ROI returned two peak intensities from the UEM image series corresponding to the two spots, BF1 and BF2, highlighted in Figure 2 (see Video S3 for a video of the UEM spatial frequency map). Overlaying the HAADF-STEM image onto the drift-corrected UEM image series using a Hough
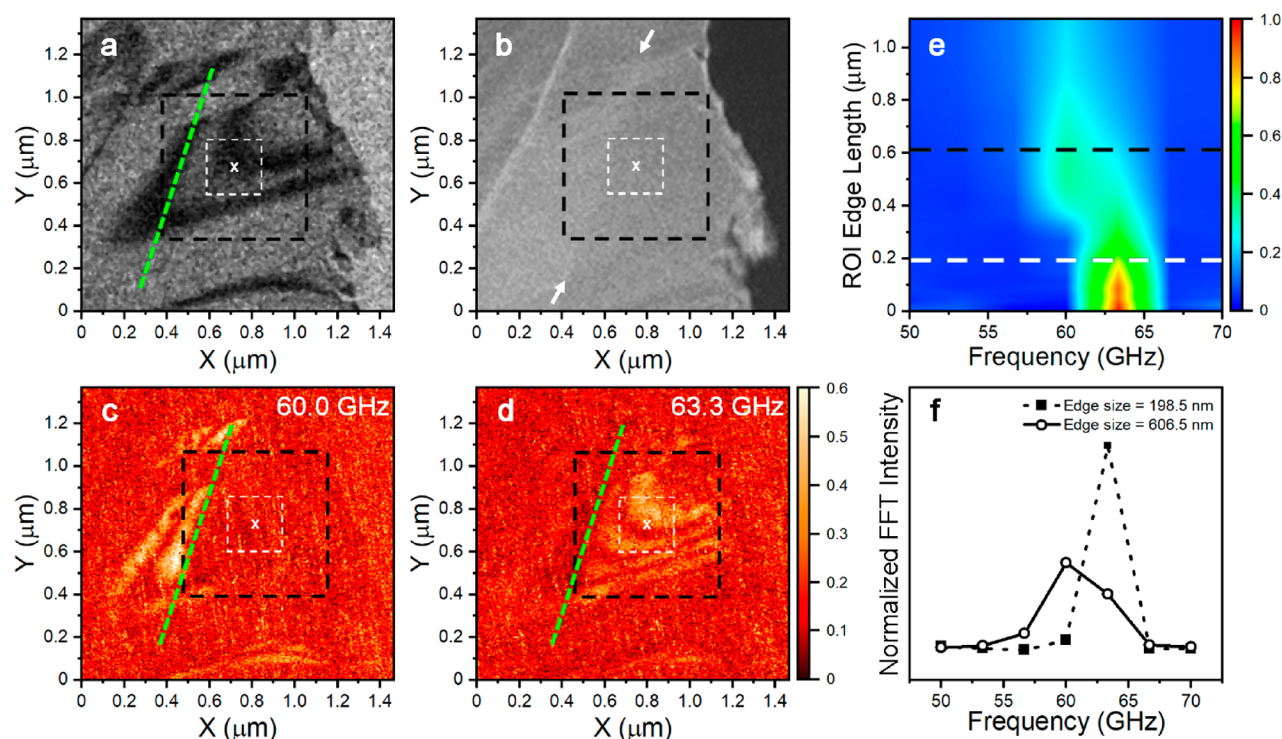
Figure 4. Demonstration of the effect of a unit-cell-height step-edge and analyzed ROI size on measured phonon dynamics in multilayer MoS_2. (a) UEM bright-field image of a freestanding MoS_2 flake. The black and white dashed squares centered on the white x mark the positions and sizes of the ROIs within which dynamics were analyzed. The green dashed line marks the approximate position of a one-unit-cell-height crystal step-edge, as determined with UEM imaging and confirmed with HAADF-STEM imaging.[11] (b) Corresponding HAADF-STEM image, with the approximate position of the step-edge indicated with two white arrows. (c, d) Spatial frequency maps of interlayer acoustic-phonon dynamics at (c) 60.0 GHz and (d) 63.3 GHz. The ROIs and step-edge location are indicated for reference. The units of the color bar are counts normalized to the maximum counts within the ROI. (e) Evolution of the FFT spectrum from the UEM image series with ROI edge length for ROIs centered at a common position [*i.e.*, the x in panels a−d]. The white and black dashed lines mark the one-dimensional FFT spectrum arising from ROIs with edge lengths of 198.5 nm and 606.5 nm, respectively. The color bar is in units of intensity normalized to the vacuum counts. (f) Plot of FFT intensity, normalized to highest intensity, as a function of oscillation frequency (GHz) for the specific ROI edge lengths highlighted with the white and black dashed lines in part e.

transform (see Supporting Information and Figures S3−S5) shows that the approximate position of the terrace is between the two frequency peak intensities (Figure 3b). This supports the hypothesis that the difference in spatial phonon frequencies is due to a difference in crystal thickness, as delineated by the 26 nm terrace. Note that the frequencies having peak intensities in the spatial frequency maps in Figure 3b (23.9 GHz in the 66 nm thick region and 16.3 GHz in the 92 nm thick region) are in good agreement with the BF1 and BF2 frequencies, respectively, determined from the UEM temporal traces summarized in Figure 2. This confirms that the peak-intensity spots in the UEM spatial-frequency maps are indeed the BF1 and BF2 spots observed in the UEM bright-field image series.

The thickness difference delineated by the crystal terrace, and the resulting spatial separation of the two observed phonon frequencies, suggests the difference in oscillation frequencies arises from different transit times of the lattice perturbation along the *c*-axis stacking direction, as opposed to two distinct low-frequency phonon modes. Indeed, from the frequencies and thicknesses, the phonon propagation speeds between the outer layers is calculated to be 3.0 ± 0.2 nm/ps and 3.1 ± 0.2 nm/ps for the 16.3 GHz and 23.9 GHz oscillation frequencies, respectively. This is markedly different from the speed along the basal plane, which was measured to be 4.2 ± 0.2 nm/ps for the specimen shown in Figure 1 and

4.7 ± 0.2 nm/ps for the specimen in Figures 2 and 3 (see the Supporting Information and Figure S6). It is important to note that all UEM experiments were conducted with the specimen initially at 300 K prior to *in situ* fs photoexcitation, and the instrument repetition rate was such that no net temperature increase occurred over the duration of the experiment. Instead, the specimen temperature increase caused by photothermal heating (estimated from the absorbance, pump fluence, specimen thickness, and specific heat capacity to be 65 K) was confined to individual pulses comprising the pump-pulse train.

As $1T$-TaS_2 is known to undergo a charge-density-wave (CDW) phase transition at 350 K (nearly commensurate to incommensurate upon heating), the relative phonon velocities measured along the different crystallographic directions may provide an indication of the connection between the bond strengths (*i.e.*, elastic properties) and the CDW phases present, without the need for separate diffraction or resistivity measurements.[32,33,36] Here, the ratio of basal-plane propagation speed to that along the *c*-axis stacking direction is 1.5 ± 0.3. Neutron-scattering measurements on bulk crystals, however, indicate the basal-plane and *c*-axis speeds of sound are similar for both the longitudinal and transverse acoustic modes at 290 K,[32] suggesting the baseline bonding anisotropy present in TMDs not displaying CDW behavior is offset in TaS_2 at temperatures where such phases are present. That is,

the enhanced interlayer interactions induced by the CDW phase effectively increases the material stiffness along the principal axis relative to the basal plane such that the speeds of sound become comparable and the ratio is approximately one at room temperature.[32,33] Evidence for this effect can be found in other TMDs displaying CDW phases, such as $TiSe_2$, $TaSe_2$, and $NbSe_2$, where the ratio of basal-plane to principal-axis sound speeds is greater than one when the CDW phase-transition temperature is exceeded (*i.e.*, the CDW phase is melted).[37−39] Accordingly, the ratio of speeds observed here may be indicative of a melting of the nearly commensurate CDW phase upon photoexcitation and possible formation of the incommensurate phase, thus producing a transient reduction in stiffness along the principal axis and a corresponding drop in phonon velocity.[40] Note, however, that another explanation may be an anomalously high basal-plane velocity arising from, for example, residual strain present from the specimen preparation method, contamination due to oxidation of the outer layers,[41] or some other source of structural or compositional variation from the stoichiometric or structurally pristine TaS_2 material. Future work will focus on reconciling these behaviors with UEM, as the emphasis here is on demonstrating the impact of discrete 2D defects, especially multilayer terraces and few-layer step-edges, on observed acoustic−phonon dynamics.

The sensitivity of UEM to the influence of local structure and morphology on phonon dynamics is particularly apparent for few-layer crystal step-edges. For example, few-GHz differences in phonon-oscillation frequencies and ps temporal dephasing of neighboring bend contours arising from a one-unit-cell step-edge in multilayer MoS_2 can be identified and resolved with UEM imaging.[11] As with the TaS_2 specimens discussed above, HAADF-STEM imaging and inspection of the UEM bright-field image series for MoS_2 reveals the approximate location of a step-edge, which again delineates two regions displaying disparate dynamics (Figure 4). Such sensitivity of ultrafast scattering methods—especially UEM imaging—to molecular-scale structural imperfections has important implications for measured responses and subsequent interpretations. This can be illustrated by simply varying the ROI size from which both temporal and frequency responses are extracted, as illustrated in Figure 4. As the size of the analyzed ROI transitions from containing only one of the observed oscillation frequencies to containing both (Figure 4a,b), the measured center of the corresponding FFT peak shifts from 63.3 GHz to 60.0 GHz (Figure 4e), while the peak fwhm and peak height increase and decrease, respectively (Figure 4f). Indeed, spatial frequency maps centered at 60.0 GHz and 63.3 GHz reveal the locations of the associated oscillatory behaviors relative to the few-layer step-edge (Figure 4c,d).

The FFT-peak broadening and decrease accompany the peak shift shown in Figure 4f because the distinct phonon-oscillation behaviors are convoluted within the select ROI. That is, if the ROI (or probe size) contains a defect (here, a step-edge) that influences the lattice response, the resulting temporal trace and associated FFT may fail to reveal the distinct dynamics. While the focus here has been mainly on real-space imaging dynamics, implications for ultrafast reciprocal-space measurements can be gleaned by noting the underlying physical principles at work. Transient elastic deformations associated with acoustic-phonon modes locally reorient the specimen relative to the incident electron wave

vector, thus altering the Bragg-scattering condition in the vicinity of the distortion. This not only produces an associated local time-varying change in image counts for the diffraction-contrast mechanism, but also an oscillatory response in the diffracted-beam counts, as illustrated above for TaS_2 (Figure 2).[6,14,15,42,43] Therefore, depending upon probe size, defect density, and defect type, responses of the Bragg spots in the diffraction pattern may be convolutions of spatially distinct structural dynamics operating on comparable time scales. Furthermore, depending upon the sensitivity of the response to the structural discontinuity, associated shifts and phase behaviors may not be resolvable—let alone spatially isolated—without imaging, potentially negating a comprehensive understanding of the spatiotemporal response of particular types of structural dynamics.

■ SUMMARY AND CONCLUSIONS

In summary, we have explicitly demonstrated the impact of two-dimensional structural defects in the form of crystal terraces and step-edges on the spatiotemporal elucidation of acoustic-phonon dynamics in TMDs, specifically $1T$-TaS_2 and $2H$-MoS_2. In TaS_2, we showed that multilayer terraces produce distinct phonon dynamics along the principal crystallographic axis, and that such dynamics can be spatiotemporally identified and resolved with UEM bright-field imaging. Furthermore, we demonstrated how the disparate signals become convoluted in reciprocal-space UEM measurements when the region containing the defect is probed using a selected-area aperture. The sensitivity of the *c*-axis phonon dynamics to a step-edge a few molecular layers in height in MoS_2 was also demonstrated, as was the capability of UEM imaging to elucidate such effects. Analogous to the UEM diffraction measurements of TaS_2, convolution of signals from disparate phonon dynamics in MoS_2 when increasing the size of the analyzed ROI was also demonstrated, and implications for both elucidating fundamental behaviors and for practical interpretation of ultrafast scattering measurements were discussed. In addition to presenting a potentially new means to probe the relationships between CDW phases and collective bonding behaviors by probing localized transient acoustic−phonon dynamics, the work reported here provides a clear demonstration of the importance of understanding the relative influence of probe size, defect density, and defect characteristics on unambiguous spatiotemporal elucidation of dynamics occurring over a common time scale.

■ ASSOCIATED CONTENT

ⓢ Supporting Information

The Supporting Information is available free of charge at https://pubs.acs.org/doi/10.1021/acs.jpca.9b12026.

> Materials and Methods, details of the three supplementary videos of UEM phonon dynamics and a UEM spatial frequency map of the oscillatory responses, and six supplementary figures of the determination of the basal-plane and *c*-axis phonon velocities, methods of edge detection, methods of image alignment, and methods of image scaling between different imaging methods and different instruments (PDF)
>
> Video S1, UEM bright-field video of basal-plane acoustic-phonon dynamics in $1T$-TaS_2 (AVI)
>
> Video S2, UEM bright-field video of *c*-axis acoustic-phonon dynamics in $1T$-TaS_2 (AVI)

Video S3, spatial frequency map generated from the UEM image series shown in Video S2 (MP4)

AUTHOR INFORMATION

Corresponding Author

David J. Flannigan − *Department of Chemical Engineering and Materials Science, University of Minnesota, Minneapolis, Minnesota 55455, United States;* orcid.org/0000-0002-1829-1868; Email: flan0076@umn.edu

Authors

Spencer A. Reisbick − *Department of Chemical Engineering and Materials Science, University of Minnesota, Minneapolis, Minnesota 55455, United States*

Yichao Zhang − *Department of Chemical Engineering and Materials Science, University of Minnesota, Minneapolis, Minnesota 55455, United States*

Complete contact information is available at:
https://pubs.acs.org/10.1021/acs.jpca.9b12026

Author Contributions

S.R. and Y.Z. contributions were formal analysis, investigation, methodology, software, validation, visualization, writing—original draft, writing—review, and editing. D.J.F. contributions were conceptualization, formal analysis, funding acquisition, methodology, project administration, resources, supervision, visualization, writing—original draft, writing—review, and editing.

Notes

The authors declare no competing financial interest.

REFERENCES

(1) Mannebach, E. M.; Li, R.; Duerloo, K.-A.; Nyby, C.; Zalden, P.; Vecchione, T.; Ernst, F.; Reid, A. H.; Chase, T.; Shen, X.; et al. Dynamic structural response and deformations of monolayer MoS_2 visualized by femtosecond electron diffraction. *Nano Lett.* **2015**, *15*, 6889−6895.

(2) Cremons, D. R.; Plemmons, D. A.; Flannigan, D. J. Femtosecond electron imaging of defect-modulated phonon dynamics. *Nat. Commun.* **2016**, *7*, 11230.

(3) Cremons, D. R.; Plemmons, D. A.; Flannigan, D. J. Defect-mediated phonon dynamics in TaS_2 and WSe_2. *Struct. Dyn.* **2017**, *4*, 044019.

(4) Mannebach, E. M.; Nyby, C.; Ernst, F.; Zhou, Y.; Tolsma, J.; Li, Y.; Sher, M.-J.; Tung, I. C.; Zhou, H.; Zhang, Q.; et al. Dynamic optical tuning of interlayer interactions in the transition metal dichalcogenides. *Nano Lett.* **2017**, *17*, 7761−7766.

(5) McKenna, A. J.; Eliason, J. K.; Flannigan, D. J. Spatiotemporal evolution of coherent elastic strain waves in a single MoS_2 flake. *Nano Lett.* **2017**, *17*, 3952−3958.

(6) Wei, L.; Sun, S.; Guo, C.; Li, Z.; Sun, K.; Liu, Y.; Lu, W.; Sun, Y.; Tian, H.; Yang, H.; et al. Dynamic diffraction effects and coherent breathing oscillations in ultrafast electron diffraction in layered 1T-TaSeTe. *Struct. Dyn.* **2017**, *4*, 044012.

(7) Le Guyader, L.; Chase, T.; Reid, A. H.; Li, R. K.; Svetin, D.; Shen, X.; Vecchione, T.; Wang, X. J.; Mihailovic, D.; Durr, H. A. Stacking order dynamics in the quasi-two-dimensional dichalcogenide 1T-TaS_2 probed with MeV ultrafast electron diffraction. *Struct. Dyn.* **2017**, *4*, 044020.

(8) Nakamura, A.; Shimojima, T.; Matsuura, M.; Chiashi, Y.; Kamitani, M.; Sakai, H.; Ishiwata, S.; Li, H.; Oshiyama, A.; Ishizaka, K. Evaluation of photo-induced shear strain in monoclinic VTe_2 by ultrafast electron diffraction. *Appl. Phys. Express* **2018**, *11*, 092601.

(9) Karam, T. E.; Hu, J. B.; Blake, G. A. Strongly coupled electron-phonon dynamics in few-layer $TiSe_2$ exfoliates. *ACS Photonics* **2018**, *5*, 1228−1234.

(10) Ideta, S.; Zhang, D. F.; Dijkstra, A. G.; Artyukhin, S.; Keskin, S.; Cingolani, R.; Shimojima, T.; Ishizaka, K.; Ishii, H.; Kudo, K.; et al. Ultrafast dissolution and creation of bonds in $IrTe_2$ induced by photodoping. *Sci. Adv.* **2018**, *4*, eaar3867.

(11) Zhang, Y.; Flannigan, D. J. Observation of anisotropic strain-wave dynamics and few-layer dephasing in MoS_2 with ultrafast electron microscopy. *Nano Lett.* **2019**, *19*, 8216−8224.

(12) Krishnamoorthy, A.; Lin, M. F.; Zhang, X.; Weninger, C.; Ma, R. R.; Britz, A.; Tiwary, C. S.; Kochat, V.; Apte, A.; Yang, J.; et al. Optical control of non-equilibrium phonon dynamics. *Nano Lett.* **2019**, *19*, 4981−4989.

(13) Tung, I. C.; Krishnamoorthy, A.; Sadasivam, S.; Zhou, H.; Zhang, Q.; Seyler, K. L.; Clark, G.; Mannebach, E. M.; Nyby, C.; Ernst, F.; et al. Anisotropic structural dynamics of monolayer crystals revealed by femtosecond surface X-ray scattering. *Nat. Photonics* **2019**, *13*, 425−430.

(14) Kwon, O.-H.; Barwick, B.; Park, H. S.; Baskin, J. S.; Zewail, A. H. Nanoscale mechanical drumming visualized by 4D electron microscopy. *Nano Lett.* **2008**, *8*, 3557−3562.

(15) Harb, M.; Peng, W.; Sciaini, G.; Hebeisen, C. T.; Ernstorfer, R.; Eriksson, M. A.; Lagally, M. G.; Kruglik, S. G.; Miller, R. J. D. Excitation of longitudinal and transverse coherent acoustic phonons in nanometer free-standing films of (001) Si. *Phys. Rev. B: Condens. Matter Mater. Phys.* **2009**, *79*, 094301.

(16) Yurtsever, A.; Zewail, A. H. 4D nanoscale diffraction observed by convergent-beam ultrafast electron microscopy. *Science* **2009**, *326*, 708−712.

(17) Yurtsever, A.; Zewail, A. H. Kikuchi ultrafast nanodiffraction in four-dimensional electron microscopy. *Proc. Natl. Acad. Sci. U. S. A.* **2011**, *108*, 3152−3156.

(18) Cremons, D. R.; Du, D. X.; Flannigan, D. J. Picosecond phase-velocity dispersion of hypersonic phonons imaged with ultrafast electron microscopy. *Phys. Rev. Mater.* **2017**, *1*, 073801.

(19) Feist, A.; Rubiano da Silva, N.; Liang, W. X.; Ropers, C.; Schäfer, S. Nanoscale diffractive probing of strain dynamics in ultrafast transmission electron microscopy. *Struct. Dyn.* **2018**, *5*, 014302.

(20) Flannigan, D. J.; Lourie, O. 4D ultrafast electron microscopy sheds light on dynamic processes from the micrometer to the atomic scale. *Microsc. Anal.* **2013**, *27*, S5−S8.

(21) Piazza, L.; Masiel, D. J.; LaGrange, T.; Reed, B. W.; Barwick, B.; Carbone, F. Design and implementation of a fs-resolved transmission

electron microscope based on thermionic gun technology. *Chem. Phys.* **2013**, *423*, 79−84.

(22) Plemmons, D. A.; Suri, P. K.; Flannigan, D. J. Probing structural and electronic dynamics with ultrafast electron microscopy. *Chem. Mater.* **2015**, *27*, 3178−3192.

(23) Feist, A.; Bach, N.; Rubiano da Silva, N.; Danz, T.; Möller, M.; Priebe, K. E.; Domrose, T.; Gatzmann, J. G.; Rost, S.; Schauss, J.; et al. Ultrafast transmission electron microscopy using a laser-driven field emitter: Femtosecond resolution with a high coherence electron beam. *Ultramicroscopy* **2017**, *176*, 63−73.

(24) Zewail, A. H. Four-dimensional electron microscopy. *Science* **2010**, *328*, 187−193.

(25) Flannigan, D. J.; Zewail, A. H. 4D electron microscopy: Principles and applications. *Acc. Chem. Res.* **2012**, *45*, 1828−1839.

(26) Adhikari, A.; Eliason, J. K.; Sun, J.; Bose, R.; Flannigan, D. J.; Mohammed, O. F. Four-dimensional ultrafast electron microscopy: Insights into an emerging technique. *ACS Appl. Mater. Interfaces* **2017**, *9*, 3−16.

(27) Pomarico, E.; Kim, Y. J.; García de Abajo, F. J.; Kwon, O. H.; Carbone, F.; van der Veen, R. M. Ultrafast electron energy-loss spectroscopy in transmission electron microscopy. *MRS Bull.* **2018**, *43*, 497−503.

(28) Egerton, R. F.; Cheng, S. C. Measurement of local thickness by electron energy-loss spectroscopy. *Ultramicroscopy* **1987**, *21*, 231−244.

(29) Malis, T.; Cheng, S. C.; Egerton, R. F. EELS log-ratio technique for specimen-thickness measurement in the TEM. *J. Electron Microsc. Tech.* **1988**, *8*, 193−200.

(30) Tanuma, S.; Powell, C. J.; Penn, D. R. Calculation of electron inelastic mean free paths (IMFPs) VII. Reliability of the TPP-2M IMFP predictive equation. *Surf. Interface Anal.* **2003**, *35*, 268−275.

(31) Schneider, C. A.; Rasband, W. S.; Eliceiri, K. W. NIH Image to ImageJ: 25 years of image analysis. *Nat. Methods* **2012**, *9*, 671−675.

(32) Ziebeck, K. R. A.; Dorner, B.; Stirling, W. G.; Schollhorn, R. Kohn anomaly in the $1T_2$ phase of TaS_2. *J. Phys. F: Met. Phys.* **1977**, *7*, 1139−1143.

(33) Frindt, R. F.; Simpson, A. M.; Jericho, M. H. Velocity of ultrasonic waves in $2H$-$NbSe_2$, $2H$-TaS_2 and $1T$-TaS_2. *Phys. Rev. B: Condens. Matter Mater. Phys.* **1980**, *22*, 4907−4914.

(34) VandenBussche, E. J.; Flannigan, D. J. Sources of error in Debye-Waller-effect measurements relevant to studies of photo-induced structural dynamics. *Ultramicroscopy* **2019**, *196*, 111−120.

(35) Frigo, M.; Johnson, S. G. The design and implementation of FFTW3. *Proc. IEEE* **2005**, *93*, 216−231.

(36) Suzuki, A.; Yamamoto, R.; Doyama, M.; Mizubayashi, H.; Okuda, S.; Endo, K.; Gonda, S. Elastic anomalies in $1T$-TaS_2. *Solid State Commun.* **1984**, *49*, 1173−1176.

(37) Moncton, D. E.; Axe, J. D.; DiSalvo, F. J. Study of superlattice formation in $2H$-$NbSe_2$, and $2H$-$TaSe_2$ by neutron scattering. *Phys. Rev. Lett.* **1975**, *34*, 734−737.

(38) Stirling, W. G.; Dorner, B.; Cheeke, J. D. N.; Revelli, J. F. Acoustic phonons in the transition-metal dichalcogenide layer compound, $TiSe_2$. *Solid State Commun.* **1976**, *18*, 931−933.

(39) Moncton, D. E.; Axe, J. D.; DiSalvo, F. J. Neutron scattering study of the charge-density wave transitions in $2H$-$TaSe_2$ and $2H$-$NbSe_2$. *Phys. Rev. B* **1977**, *16*, 801−819.

(40) Givens, F. L.; Fredericks, G. E. Thermal expansion of $NbSe_2$ and TaS_2. *J. Phys. Chem. Solids* **1977**, *38*, 1363−1365.

(41) Tsen, A. W.; Hovden, R.; Wang, D.; Kim, Y. D.; Okamoto, J.; Spoth, K. A.; Liu, Y.; Lu, W.; Sun, Y.; Hone, J. C.; et al. Structure and control of charge density waves in two-dimensional $1T$-TaS_2. *Proc. Natl. Acad. Sci. U. S. A.* **2015**, *112*, 15054−15059.

(42) Park, H. S.; Baskin, J. S.; Barwick, B.; Kwon, O. H.; Zewail, A. H. 4D ultrafast electron microscopy: Imaging of atomic motions, acoustic resonances, and moire fringe dynamics. *Ultramicroscopy* **2009**, *110*, 7−19.

(43) Cremons, D. R.; Schliep, K. B.; Flannigan, D. J. Diffraction contrast as a sensitive indicator of femtosecond sub-nanoscale motion

in ultrafast transmission electron microscopy. *Proc. SPIE* **2013**, *8845*, 884507.